Defects in MgB_4O_7 (pure and doped with lanthanides): a case study using a computational modelling approach.

Giordano F. C. Bispo[1], Débora S. Nascimento[2], Lucas B. Santana[3], Gilvan S. Ferreira[4], Hestia R. B. R. Lima[4], Susana O. Souza[3], Francesco d'Errico[2,5], Robert A. Jackson[6], Mário E. G. Valerio[1,3]

[1] Materials Science and Engineering Department, Federal University of Sergipe, 49100-000, São Cristovão, SE, Brazil

[2]Department of Civil and Industrial Engineering, University of Pisa, Largo Lazzarino 1, 56122 Pisa, Italy.

[3] Physics Department, Federal University of Sergipe, 49100000 São Cristovão, SE, Brazil

[2] Instituto Federal de Sergipe, campus Lagarto, 49400000 - Lagarto, SE, Brasil
[5] School of Medicine, Yale University, New Haven, CT, USA

[6] School of Chemical and Physical Sciences, Keele University, Keele, Staffordshire, ST5 5BG, UK

(Correspondent author: gfredericoc@gmail.com)

ABSTRACT: Lanthanide-doped MgB4O7 is a potential dosimetry due to its thermoluminescence (TL) and optically stimulated luminescence (OSL) properties. These properties have been largely reported, but there are few theoretical studies dedicated to understanding the material defects. The aim of this work is to demonstrate that defects are a key issue to understand the luminescent mechanisms. A new set of interatomic potential parameters were obtained reproduced MgB4O7 structure better than 2% and 4% for oxide precursors. The results showed that the O Frenkel defect is the most probable which can account for the intrinsic blue emission in undoped material. Also, the extrinsic defect calculations demonstrated two possible doping schemes for lanthanide ions. One lanthanide dopant group prefers the direct substitution in boron site with a molecule of (BO3)-3 moving to balance the strain caused by this substitution. Another prefers a substitution in magnesium site with an MgB anti-site as charge compensation defect.

Keywords: Magnesium tetraborate, Atomistic Computational Modelling, intrinsic defects, extrinsic defects.

I. INTRODUCTION

Magnesium tetraborate (MgB_4O_7) is a phosphorus studied since the early 1980s because of its TL and OSL properties when doped with lanthanides [1–4]. Recently, some works proposed that this material is also sustainable for application as a passive temperature sensor [5,6]. The interest in the MgB_4O_7 dosimetric properties is because this borate presents an effective atomic

number (Zeff = 8.2) like tissue (Zeff = 7.35–7.65), which is excellent for use in personal dosimetry due to its lack of correction factors for dose calculations [7]. Moreover, the material is sensitive to photons and charge particles with linear response in a wide absorbed dose range, from mGy up to 100 Gy [8]. The presence of boron in the matrix also allows the substitution of natural boron source by B^{10} and B^{11} enriched sources with high capture cross-section for thermal neutrons. In recent years, this fact has been explored as a possible solution for measuring in-vivo dose for patients in radiotherapy treatments and in Boron Neutron Capture Therapy (BNCT) as well as human activities during the nuclear fuel cycle [9].

Although MgB_4O_7 has a vast literature dedicated to dosimetry properties obtained using TL and OSL, there is a lack of knowledge about the luminescent mechanism responsible by TL/OSL emissions. Moreover, there are few theoretical papers dedicated to understanding the basic properties of the defects in the material from the computational modelling point of view [10]. But, as a dosimeter, the material is exposed to the radiation field and the primary effect that is used in almost all types of dosimetric measurements are related to the defects already present and the ones generated by the interaction of the radiation with the material. Consequently, the knowledge of the physical and chemical properties of the defects that may be present in any dosimetric material is a key issue to understand the mechanisms behind the dosimetric signals and is also very important to improve the quality of the dosimeter.

Systematic studies carried out with lanthanide (Ln) doped MgB_4O_7 samples have already shown that different dopants are associated with different luminescence mechanisms [11,12], and there is a possibility that the intrinsic and extrinsic defects are related to the light emissions and electron paramagnetic resonance signals [13,14]. These features can be studied through classical computational modelling which is based on interatomic potentials and lattice energy minimisation [15,16]. Classical modelling allows the study of several configurations for intrinsic defects as well as doping schemes with a low computational cost. This methodology has been successfully used to predict the most probable defects in materials solving some open experimental questions [16–18].

The present work proposes to predict the most likely intrinsic defects as well as studying defects created by insertion of lanthanide dopants in the MgB_4O_7 matrix. Such results can contribute to the completely understanding of the luminescent mechanisms in the dosimetry radiation field. The first challenge for these goals is fitting a set of interatomic potential parameters for the structure, mainly for borate-based structures where these parameters are not

well established. The second step will be to calculate all intrinsic and extrinsic defects. Finally, the comparison with experimental results will lead to a complete understanding of results and will provide further evidence that can be used to propose a model for the luminescence emission of the material.

II. METHODOLOGY

The computational atomistic modelling applied in this work is based on interatomic potentials and lattice energy minimisation. This classical approach has been successfully applied in ionic and covalent materials yielding important understanding of defect behaviour [16,19–21]. Three basic steps are followed to model defects through this method: the first step is to obtain an interatomic potential set using previously derived potentials or by deriving a special set to model the material in focus. Next, all defects in the material and the corresponding mechanisms are established to compute the energetics of the defects in terms of solid-state reactions. The last step is calculating the energy terms involved in the reactions [17]. the General Utility Lattice Program (GULP) was used to perform all calculations [22].

For the first step it is necessary to know which atomic bond is related to the interatomic potential set. MgB_4O_7 has an orthorhombic structure belonging to space group Pbca (see figure 1) [23]. The unit cell presents one magnesium non-symmetric site with five neighbouring oxygen polyhedra (orange polyhedra) linked to $(B_4O_9)^{-6}$ basic repeating blocks via corner-linked oxygens [10]. The boron block is divided in four non-symmetric sites: B1 and B3 with tetrahedral coordination of four neighbouring oxygens (blue polyhedra) and B2 and B4 with planar trigonal oxygen coordination (green polyhedra). There also are seven oxygen non-symmetric sites. Looking at the structure along the c-axis (see Figure 1) is possible to see a region where atomic distances are far enough apart to include interstitial ions.

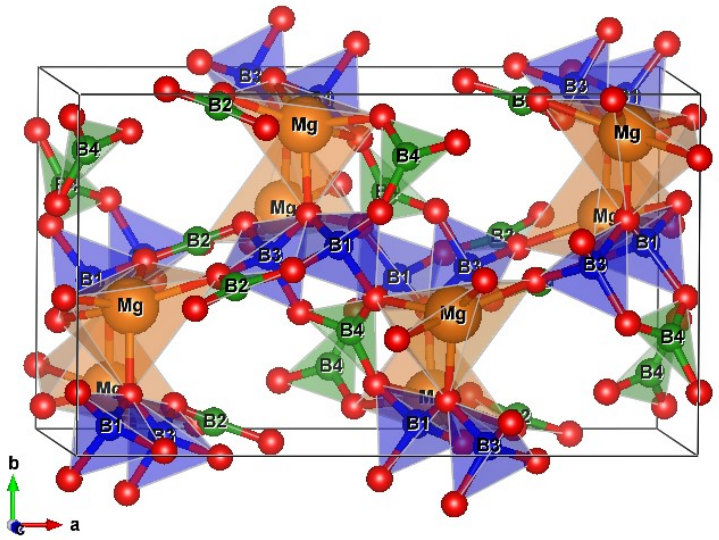

Figure 1 – Crystal structure of MgB_4O_7 reproduced using the VESTA program [23] using lattice parameters from #34397 ICSD card [23].

The Coulomb potential supplemented by a Buckingham potential is commonly used to describe ionic interactions while for covalent ones usually Morse and many-body potentials are used [17,25]. An analysis of DOS calculations has concluded that Mg-O bonds are ionic while B-O bonds have a covalent character due to hybridization of the B and O states in MgB_4O_7 [10]. Therefore, it is usual to assume that interactions between rare earth and magnesium with oxygen are described by ionic pair-potentials while boron-oxygen will require an additional covalent term.

The set of pair-potential parameters used in the present work for Ln-O bonds are well established [19]. Otherwise, there are few set of potential parameters for B-O bonds in the literature used to describe B_2O_3 structures [24,25], however, they did not provide a consistent description of MgB_4O_7 crystalline structure and bulk properties. Therefore, a new set of potential parameters had to be derived to ensure the best reproduction of MgB_4O_7 structure and the B_2O_3 and MgO oxide precursors. A Buckingham type potential was used to describe B-O pair interactions and a three-body bond-bending term was added to ensure the reproduction of the B-O-B bond angles. MgB_4O_7 presents two borate groups, $(BO_4)^{5-}$ tetrahedra and $(BO_3)^{-3}$ triangles, which have different bond angles, requiring two types of three-body terms for a correct description of the crystalline structure. Unlike some previous publications, we considered the trivalent oxidation state for B following the nominal state for B_2O_3 precursor. Such considerations allow many defects to be calculated including a substitution of boron ion by one trivalent rare earth element.

Based on previous experience and the literature, a good set of potential parameters reproduces lattice parameters with discrepancy within ±2% for the main structure and ±5% for oxide precursors [18]. The set of potential parameters was fitted to reproduce the experimental structures and properties as accurately as possible requiring an additional fit to the Mg-O pair-potential available in the literature to ensure the best reproduction of the MgB_4O_7 structure. The potential parameters can be seen in table 1 while the comparison between experimental and calculated crystal lattice parameters for and MgB_4O_7 and the oxide precursors are showed in table 2. All calculated lattice parameters differences are within acceptable limits, lower than 2% for MgB_4O_7 and around 3% for both MgO and B_2O_3.

Table 1 - *Parameters of the potentials used for crystal lattice modelling.*

Buckingham (Cut-offs = 10 Å)			
Interaction	**A_{ij}[eV]**	**ρ_{ij} [Å]**	**C_{ij} [eVÅ^6]**
Mg-$_{core}$- O-$_{Shell}$	946.63	0.3081	0.000
B-$_{core}$- O-$_{Shell}$	567.29	0.3324	0.000
O$_{Shell}$- O$_{shell}$	22764.0	0.1490	27.879
Three body terms (Cut-offs = 1.8, 1.8, 3.2 Å)			
Interaction	**K[eVrad^{-2}]**	**θ(rad)**	
B1$_{core}$-O$_{shell}$-O$_{shell}$	4.09724	109.4	
B2$_{core}$-O$_{shell}$-O$_{shell}$	2.09724	120.3	
Shell model (eVÅ^{-2})			
Spring O$_{shell}$-O$_{shell}$	70.0		
Charge of the ions [e]			
Mg$_{core}$	**B$_{core}$**	**O$_{core}$**	**O$_{shell}$**
2.00000	3.00000	0.86902	-2.86902

Table 2 - *Comparison between experimental and calculated crystal lattice and oxide precursor parameters at 0 K.*

Parameter	**Experimental**	**Calc. 0 K**	**Δ%**
	MgB_4O_7 [23]		
a	13.730000	13.848758	0.86
b	7.970000	8.101029	1.64
c	8.620000	8.671833	0.60
α=β =γ	90.0	90.0	0.00
	B_2O_3 [27]		
a=b	4.335900	4.308210	0.64

c	8.342000	8.104961	2.81
α=β	90.0	90.0	0.00
γ	120.0	120.0	0.00
	MgO [28]		
a=b=c	4.217000	4.074932	3.37
α=β =γ	90.0	90.0	0.00

Another aspect that should be considered is the Gibbs free energy for the formation of the MgB_4O_7 structure. From a theoretical point of view, the Gibbs free energy represents the stability of a crystal under a specified thermodynamic condition. The crystal is stable under those temperature and pressure conditions if $\Delta G_{formation}$ is negative, otherwise the segregation of the precursors happens. Equation 1 shows the solid-state reaction that describes the formation of magnesium tetraborate from precursor oxides as well as Gibbs free energy calculations:

$$MgO + 2B_2O_3 \rightleftarrows MgB_4O_7$$
$$\Delta G_{formation} = E^{Latt}_{MgB_4O_7} - E^{Latt}_{MgO} - 2E^{Latt}_{B_2O_3} \quad (1)$$

Table 3 shows the lattice energy for MgB_4O_7 and lattice energy for precursor oxides as well as the negative Gibbs free energy calculated.

Table 3 - *Lattice energy calculated for MgB_4O_7 and their precursor oxides and free Gibbs formation energy at 0K.*

Material	Lattice Energy[eV]
MgO [28]	-42.04
B_2O_3 [27]	-175.86
MgB_4O_7 [23]	-394.51
$\Delta G_{formation}$	-0.75

Lastly, the set of potential parameters need to reproduce the bond distances and angles in the B-O polyhedra for MgB_4O_7 structure. It is highlighted here that the three-body potential, acting on the O-B-O angle, was added to preserve the arrangement of two borate groups on the B-O polyhedra. Thus, a good potential set must reproduce both B-O polyhedrons keeping final

values of the bond distances and angles in the simulated structure close to the values obtained experimentally. Results given in table 4 shown that the simulated B-O distance in the polyhedra are below 3.57% of the expected experimental values while the simulated bond angles were w 4.31% as compared to the values calculated from the experimental determined MgB_4O_7 crystalline structure. These results shown that new set of potential parameters are consistent in reproducing the MgB_4O_7 structure.

Table 4 - *Comparison between average experimental and calculated distances in borate polyhedra at 0 K.*

Polyhedron	***Site***	**Experimental [23]**	**Simulated**	**Δ%**
$(BO)_4$	B1	1.4697	1.5042	2.35
	B3	1.4789	1.5141	2.38
$(BO)_3$	B2	1.3632	1.4067	3.19
	B4	1.3624	1.4111	3.57

Table 5 - *Comparison between experimental and calculated angles in borate polyhedra.*

Polyhedron 1 $(BO)_4$			
Angle	Experimental[23]	Simulated	Δ%
Φ_1	108.9	107.8	1.01
Φ_2	108.9	110.8	1.74
Φ_3	119.4	119.6	0.17
Φ_4	105.8	105.5	0.28
Φ_5	110.8	110.8	0.00
Φ_6	103.4	100.4	2.90
Polyhedron 2 $(BO)_3$			
Θ_1	120.1	124.7	3.83
Θ_2	119.1	119.8	0.59
Θ_3	120.6	115.4	4.31

Having obtained the set of potential parameters, the next step is to calculate the formation energy to create each isolated point defect in MgB_4O_7 structure. The calculations were performed by the Mott-Littleton method, which can provide a concentration of defects in the dilute limit. This method consists in separate defect calculus in two spherical regions. For the first region, defects are treated considering all interactions (region I) evaluating all position parameters, while more distant parts are treated using a continuum approach (region II). Lattice induced distortions by the defect are treated through region II division. For region II(a) each ion displacement is calculated considering an harmonic approximation. The region II(b) is considered a dielectric continuum, since the influence of the defect is very small [18]. Several

region sizes were tested and a consistent cut-off radius of 15 and 19 Å for region I and II(a), respectively, was found for intrinsic and extrinsic defects.

The formation energies were calculated for all non-symmetrical equivalent site positions in MgB_4O_7 structure: 7 positions for oxygen, 4 for boron and 1 for magnesium. They are used to calculate vacancy point defects. Furthermore, 4 interstitial positions were found by inspecting the empty volumes in the unit cell and considering a minimum distance of from the first neighbours, and they are presented in table 6. These positions were used to calculate interstitial point defects.

Table 6 - *Coordinates of the interstitial positions*.

P1	0.0 0.0 0.0
P2	1/2 1/2 1/2
P3	1/4 1/4 1/2
P4	1/4 1/4 1/4

The formation energies of isolated point defects (vacancies, interstitials, and doping substitution) allow numerous defect configurations. This is one of the advantages of atomistic classical modelling because it is possible to cover all defect configuration without a huge computational cost. Also, this methodology can give an idea about the atomic positions close to defect region before and after the lattice relaxation that helps the luminescence phenomena interpretation.

III. RESULTS AND DISCUSSION

Intrinsic defects

The determination of energies for Frenkel, Schottky and others type of intrinsic defects can provide a good estimate about what occurs in undoped material. They are obtained through a combination of isolated point defect (vacancy and interstitial) energies and relevant lattice energies calculated previously. For example, an oxygen Frenkel pair is a combination of an oxygen vacancy and one oxygen interstitial ion. In this case, there are seven different oxygen sites for vacancies and each one of them were calculated separately. In additional, there are four different interstitial positions calculated separately that yield 28 combinations of unbound

oxygen Frenkel pairs. Reactions for these defects are showed in table 7, represented in Kröger–Vink notation, as well as the lowest energy value found for each defect. Solution defect energies were calculated using lattice energies presented in table 3. Energies obtained are normalised by number of point defects necessary in each reaction. They are calculated under the unbound condition, where it assumes basic defects are so far apart that there is no interaction between the basic constituents of the constituents of the considered intrinsic disorder [12].

Table 7 - *Reaction schemes (defect equations) and values of lowest solution energies for intrinsic defects in MgB_4O_7 calculated under unbound condition.*

Scheme	Defect equations	Solution energy [eV/Defect]
(i)	$B_B \rightarrow B_I^{\bullet\bullet\bullet} + V_B^{'''}$	5.50
	$E_{sol} = E_{B_I^{\bullet\bullet\bullet}} + E_{V_B^{'''}}$	
(ii)	$Mg_{Mg} \rightarrow Mg_I^{\bullet\bullet} + V_{Mg}^{''}$	2.48
	$E_{sol} = E_{Mg_I^{\bullet\bullet}} + E_{V_{Mg}^{''}}$	
(iii)	$O_O \rightarrow O_I^{''} + V_O^{\bullet\bullet}$	2.05
	$E_{sol} = E_{O_I^{''}} + E_{V_O^{\bullet\bullet}}$	
	Pseudo-Schottky	
(iv)	$2B_B + 3O_O \rightarrow 2V_B^{'''} + 3V_O^{\bullet\bullet} + B_2O_3$	2.72
	$E_{sol} = 2E_{V_B^{'''}} + E_{V_O^{\bullet\bullet}} + E_{B_2O_3}^{Latt}$	
(v)	$Mg_{Mg} + O_O \rightarrow V_{Mg}^{''} + V_O^{\bullet\bullet} + MgO$	3.13
	$E_{sol} = E_{V_{Mg}^{''}} + E_{V_O^{\bullet\bullet}} + E_{MgO}^{Latt}$	
	Schottky	
(vi)	$Mg_{Mg} + 4B_B + 7O_O \rightarrow V_{Mg}^{''} + 4V_B^{'''} + 7V_O^{\bullet\bullet} + MgB_4O_7$	2.73
	$E_{sol} = E_{V_{Mg}^{''}} + 4E_{V_B^{'''}} + 7E_{V_O^{\bullet\bullet}} + E_{MgB_4O_7}^{Latt}$	
	Anti-Schottky	
(vii)	$MgB_4O_7 \rightarrow Mg_I^{\bullet\bullet} + 4B_I^{\bullet\bullet\bullet} + 7O_I^{''}$	3.58
	$E_{sol} = E_{Mg_I^{\bullet\bullet}} + 4E_{B_I^{\bullet\bullet\bullet}} 7E_{O_I^{''}} - E_{MgB_4O_7}^{Latt}$	

Results from Table 7 show that the oxygen Frenkel pair, a combination of an O ion in an interstitial site and a O vacancy, is the most favourable intrinsic defect while Boron Frenkel pair has the highest energetic cost. There are a few reports which show emissions in undoped samples from an unknown centre [8,12,29]. These emissions ranged from near-UV up to blue spectral region and could be assigned to some intrinsic defect like F-centres or self-trapped excitons (STE) [30]. The STE emissions are strongly temperature dependent, usually occurring at temperatures below 150 K, which is not the case for these reports. Moreover, intrinsic emission reported by Souza et. al. is obtained under 315 nm excitation, far below the predicted

MgB_4O_7 band gap [8,10]. Thus, there is a probability that these emission bands arise from an O centre defect such as an F-centre (electrons trapped in an oxygen vacancy). This argument is reinforced by an electron paramagnetic resonance (EPR) study where signals assigned as an electron trapped at oxygen ion vacancy were reported in a Tm-doped MgB_4O_7 sample [13].

Until now, defects were calculated under an unbound condition that gives an idea about the energetic cost of the defect but cannot address how structure changes with intrinsic disorder. In order to access this information, all constituents of the defect should be added in the same unit cell including explicitly the interaction among the basic defects. This is known as the bound condition [17].

There are some aspects that should be considered to choose the starting configurations for the simulations of oxygen Frenkel pairs. The vacancy and interstitial positions should be far enough apart to avoid the interstitial ion returning to the vacancy position. In the calculations presented in this work. a minimum distance between them of 2 Å was considered. However, the distances between the two constituents are not expected to be so far apart since they are both charged defects and one should expect that the Coulombic attraction will pull together the O vacancy and interstitial. The initial configurations of oxygen Frenkel pair as well as solution energies obtained are presented in Table 8.

Table 8 - *Values of lowest solution energies and pair distance for oxygen Frenkel defects under bounded condition in the MgB_4O_7. The values were normalized to the total number of basic defects.*

Vacancy Crystallographic Site	Interstitial position							
	P1		P2		P3		P4	
	E_{sol}(eV)	D (Å)	E_{sol}(eV)	D (Å)	E_{sol}(eV)	D (Å)	E_{sol}(eV)	D (Å)
O_1	2.37	4.615	2.43	2.842	1.81	3.961	1.87	6.807
O_2	3.18	3.484	1.41	2.305	1.30	2.538	1.25	2.282
O_3	5.76	4.341	*nc*	3.695	5.80	3.498	1.03	3.625
O_4	2.34	5.584	1.96	3.964	5.58	6.721	0.90	2.703
O_5	1.73	3.735	1.54	3.790	3.80	2.336	1.78	4.150
O_6	3.21	7.170	2.71	3.956	*nc*	4.230	*nc*	3.624
O_7	3.74	5.455	1.91	5.126	3.02	5.835	1.14	9.139

The solution energies found are typically lower than its similar Frenkel pairs calculated under unbounded condition. This is expected because the interaction among the basic defects is explicitly included [17]. Apart from being a more realistic modelling approach, close to what is expect to happen in a real crystal, another advantage of the bound defect simulation is that the final configuration of the lattice around the defect after the lattice relaxation is readily available. Figure 1 shows the comparison of the crystalline lattice in the neighbourhood of the

O Frenkel pair disorder before and after the lattice relaxation for the lowest energetic Frenkel pair configuration according to the results shown in table 7.

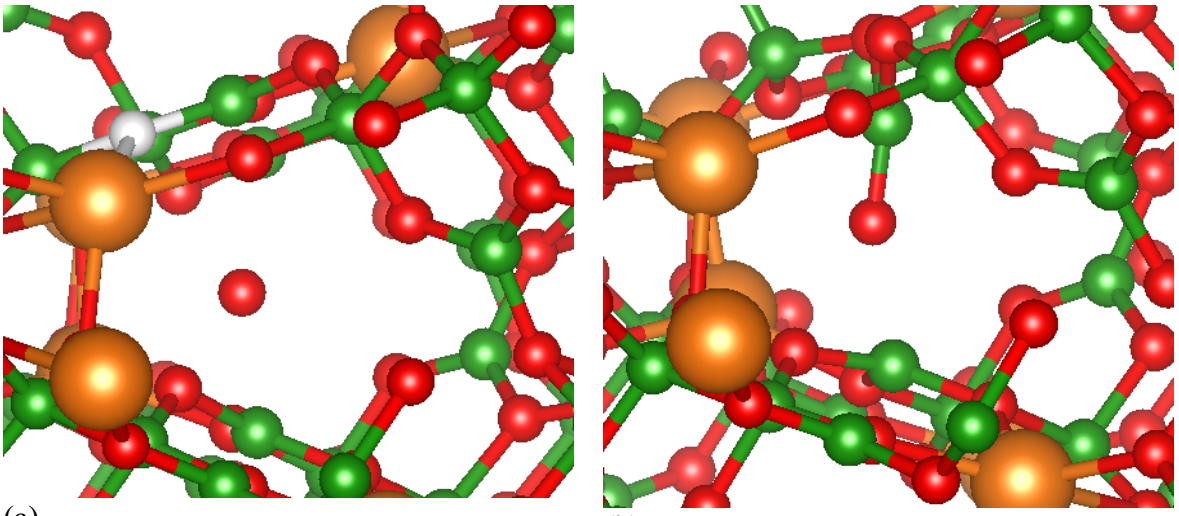

(a) (b)

Figure 2 - Configuration with lowest energetic cost for a bound O Frenkel pair defect. It can be observed that the crystallographic oxygen vacancy site, shown as a grey shaded sphere, is the one that links boron and magnesium ions, while interstitial atom is in the middle of an empty region of the crystal. (a) represents the geometry of the lattice before relaxation while (b) shows the final position of the neighbouring ions after relaxation of the lattice.

Figure 2(a) shows the region of Frenkel pair defect before relaxation. The interstitial position P4 (1/4 1/4 1/4) is in middle of an empty region in material while the O4 crystallographic site (represented by a grey-shaded sphere) is surrounded by two boron and one magnesium ion. This atom links two different polyhedra of boron (BO_4, BO_3) and the magnesium polyhedra. When the vacancy is created the BO_4 becomes a BO_3 while BO_3 changes to a BO_2. The BO_2 molecule is unstable and will need an extra oxygen ion to stabilise itself. In this case, the interstitial oxygen originally sitting at the P4 position, is pulled close to the unstable BO_2 group, as shown in figure 2(b), that represents the lattice after relaxation. The vacancy region shows that the surrounding atoms undergo some electric field effect due to basic defects, but interstitial oxygen stabilises them without large modifications.

The existence of a stabilised Frenkel pair opens possibilities for understanding the TL and OSL mechanisms and reinforces the F-centre luminescent emission hypothesis. However, the TL peak in the undoped material has been assigned to impurity ions present in precursors and not to the presence of intrinsic defects [31]. It could occur if the energy levels created by Frenkel pair defect are too shallow or deep for usual TL temperature region or electron-hole

pair recombination yields a photon in emission not detectable by a typical TL and OSL light detection systems. However, it is important to consider in TL mechanisms the possibility of F-centres and hole trapped created by interaction between an interstitial oxygen and a BO_3 molecule.

Extrinsic defects

Although an intrinsic defect study can be useful for understanding of luminescent properties in this material, most reports have been dedicated to Ln-doped MgB_4O_7 samples. The lanthanides (Ln) elements have been used as common dopants aiming the improve of the thermoluminescent intensity by many researchers since these elements are known as an effective way to obtain excellent luminescence properties [32]. Several reports have pointed out the Mg crystallographic site as a unique substitutional site because B-O would be a strong covalent bond [10,29,32]. Although may sound reasonable, there is no direct evidence that the Ln dopant ions actually substitute only for the Mg ions in the matrix and there is no work in the literature that test the hypothesis that maybe B sites can also accommodate Ln-doped ions. One of the aims of the present work is to test all cationic possibilities for Ln^{3+}-doping substitutions and let the energetic costs of the possible defect to decide which would be the main mechanism for Ln incorporation in the matrix.

The solid-state reactions used to calculate the Ln^{3+} extrinsic defects are presented in table 9 as well as the corresponding solution energy equations. These reactions simulate the probable defects created by substitution of one Ln^{3+} ion in a cationic host site taking account all possible charge compensation mechanisms when needed. The isovalent boron substitution (i) is only possible because the set of potential parameters used in this work consider the formal charge for boron ion. For aliovalent substitution at Mg^{2+} sites, the compensation mechanisms were tested considering Mg anti-site defect (ii), oxygen interstitials (iii), magnesium and boron vacancies (iv and v). Having these reactions, the solution equations can be constructed using lattice energies presented in table 3 and reference [19].

Table 9 - *Reaction schemes and solution energy defect equations for extrinsic defects in MgB_4O_7. In these expressions E_{sol} , E_{def} and E_{latt} are solution, formation defect and lattice energies, respectively.*

(i)	$\frac{1}{2}\ \mathrm{Ln_2O_3}+\mathrm{B}_B \rightarrow \mathrm{Ln}_B+\frac{1}{2}\ \mathrm{B_2O_3}$
	$\mathrm{E}_{sol}=\mathrm{E}_{def}+\ \frac{1}{2}\ \mathrm{E}^{Latt}_{B_2O_3}\ -\ \frac{1}{2}\ \mathrm{E}^{Latt}_{Ln_2O_3}$
(ii)	$\frac{1}{2}\ \mathrm{Ln_2O_3}\ +\ \mathrm{Mg}_{Mg}\ +\ \mathrm{B}_B \rightarrow \left(Ln^{\bullet}_{Mg}-Mg^{'}_{B}\right)\ +\frac{1}{2}\ \mathrm{B_2O_3}$
	$\mathrm{E}_{sol}=\mathrm{E}_{def}+\ \frac{1}{2}\ \mathrm{E}^{Latt}_{B_2O_3}\ -\ \frac{1}{2}\ \mathrm{E}^{Latt}_{Ln_2O_3}$
(iii)	$\mathrm{Ln_2O_3}+2\mathrm{Mg}_{Mg} \rightarrow \left(2Ln^{\bullet}_{Mg}-O^{''}_{i}\right)\ +2\mathrm{MgO}$
	$\mathrm{E}_{sol}=\mathrm{E}_{def}+2\mathrm{E}^{Latt}_{MgO}-\mathrm{E}^{Latt}_{Ln_2O_3}$
(iv)	$\mathrm{Ln_2O_3}+3\mathrm{Mg}_{Mg} \rightarrow \left(2Ln^{\bullet}_{Mg}-V^{''}_{Mg}\right)\ +3\mathrm{MgO}$
	$\mathrm{E}_{sol}=\mathrm{E}_{def}+3\mathrm{E}^{Latt}_{MgO}-\mathrm{E}^{Latt}_{Ln_2O_3}$
(v)	$\frac{3}{2}\ \mathrm{Ln_2O_3}\ +\ 3\mathrm{Mg}_{Mg}\ +\ \mathrm{B}_B \rightarrow \left(3Ln^{\bullet}_{Mg}-V^{'''}_{B}\right)\ +3\mathrm{MgO}\ +\frac{1}{2}\ \mathrm{B_2O_3}$
	$\mathrm{E}_{sol}=\mathrm{E}_{def}+\ 3\mathrm{E}^{Latt}_{MgO}\ +\ \frac{1}{2}\ \mathrm{E}^{Latt}_{B_2O_3}\ -\ \frac{3}{2}\ \mathrm{E}^{Latt}_{Ln_2O_3}$

The interactions of the lanthanide ions were described through a set of pairwise interatomic potentials derived previously in [19]. Formation energies for Ln substitution were calculated for all symmetrically non-equivalent cationic sites, and formation energies previously calculated for isolated point defects were used. There is no strict rule about insertion of dopant in the host material, however defects involving ions of similar nature (ionic radius, charge, and bonds) tend to have small energetic cost [16].

The plot of solution energies per defect versus ionic radii is important because it shows the tendency of more favourable substitution comparing ionic radii and kind of defect involving in solutions. Figure 3(a) presents values of the lowest solution energies as a function of each ionic radius for the unbound condition while Figure 3(b) shows the same for the bound condition. It is important to highlight that all positions and defects were considered in assuming the bound condition.

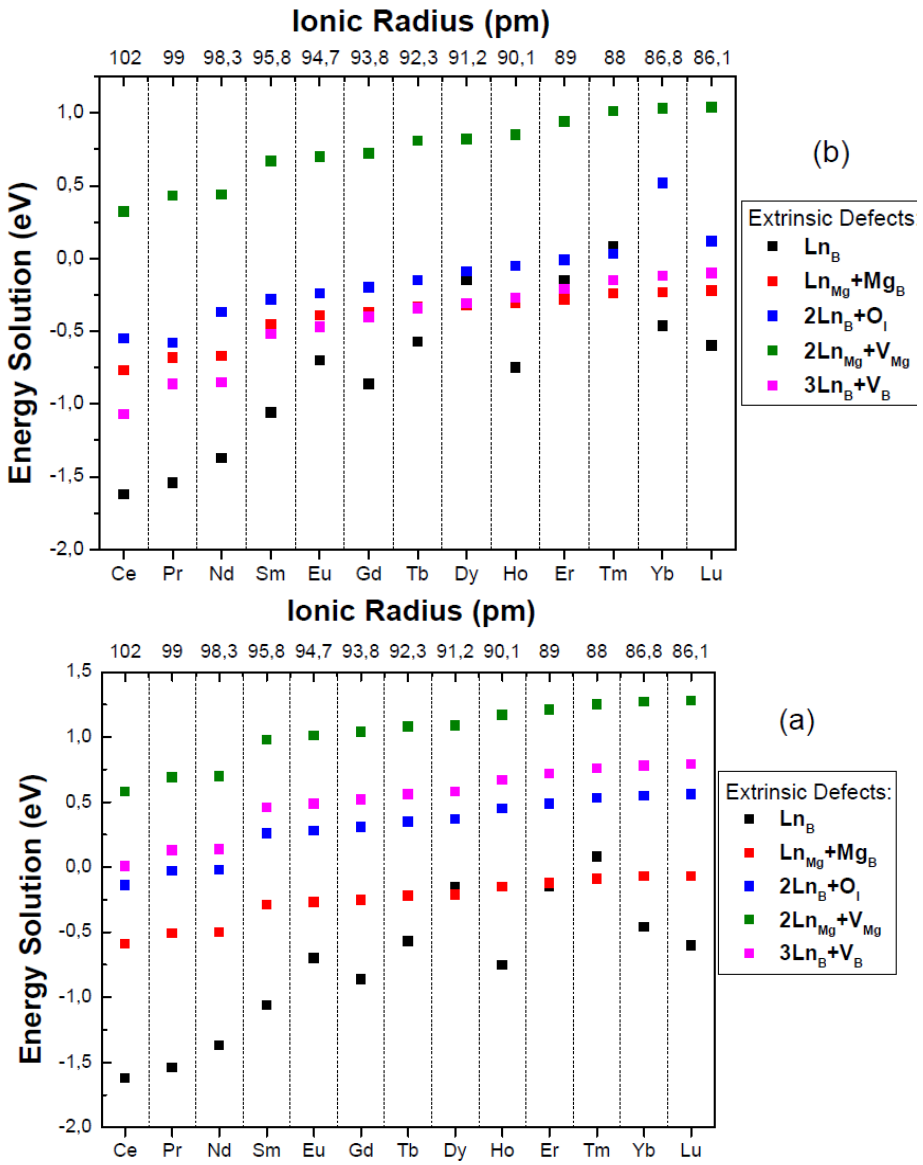

Figure 3 - Plot of lowest solution energy for each scheme represent in Table 9 as function of ionic radii calculated under (a) unbound and (b) bounded condition. All energies were normalised by number of point defects. Values for reaction scheme (i) are identical for both conditions.

Typically, defects calculated under unbound condition have higher energetic cost than bound ones because the Coulomb term acts as an attraction term while lattice strain can be contributed positively or negatively to the energy. In fact, the energetic cost of lattice strain due to introduction of dopant will determine which defect configuration is the most favourable for that system. Results in figure 3 show that all solution energies calculated under unbound conditions have an energetic cost by defect higher than the corresponding bound case. For both cases, the solution energies decrease with ionic radii increasing for all compensation mechanism schemes (ii - v) while isovalent substitution (scheme i) displayed a maximum

energetic cost for Tm and Er dopant ions, decreasing after that as the Ln ionic radius also decreased. It is important to note that the isovalent substitutions at the boron site does not have "bound" and unbound" configuration since the defect involved only the Ln substituting for the B in a particular lattice site, as discussed previously.

Some works have suggested Mg sites as more appropriate sites for impurity substitution, even in the case large dopant ions [10,29,32], yielding a necessary charge compensation mechanism. Results in figure 3(b) suggests that this maybe be the case for Tm, Er and Dy dopant ions where the substitution in Mg sites with a Mg anti-site located in trigonal B site as compensation mechanism was the most favourable defect. However, for most of Ln ions (Lu, Yb, Ho, Tb, Gd, Eu, Sm. Nd, Pr and Ce), a direct substitution at one of the B sites is the less energetically expensive defect. These results may sound unexpected taking account the nature of bonding and the significant difference between lanthanides and boron environment.

Looking all dopant schemes proposed (table 9), we can observe that reactions where there is a reduction of boron quantities in the final product have less energetic cost than Mg sites and interstitial oxygen (figure 3). Such a fact does not mean that boron oxygen bounds are weak, but that the material prefers a substitution where degree of ionicity increases. Also, it suggests that synthesis with reduction of boron source quantities while rare earth dopant quantities increase can favour the doping. In the literature, doped and codoped MgB_4O_7 is synthesized reducing host quantities or using excess of boric acid to achieve the correct crystalline phase [11]. This stoichiometric deviation is observed in several works and can be linked with boron molecule release when material is doped, but further studies are necessary to prove this.

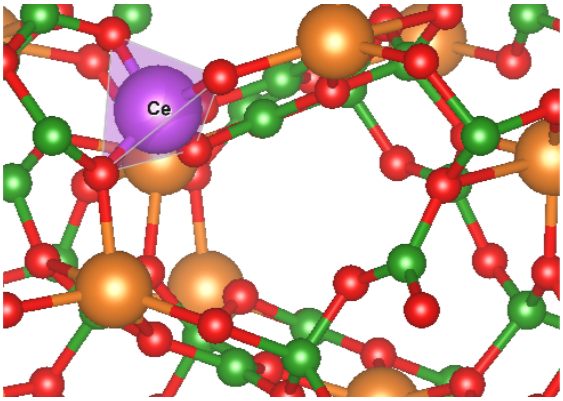

(a)

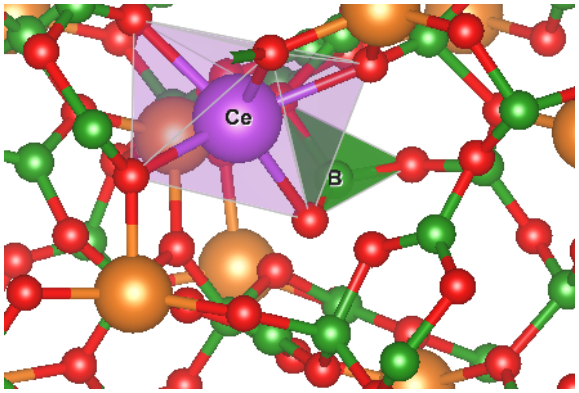

(b)

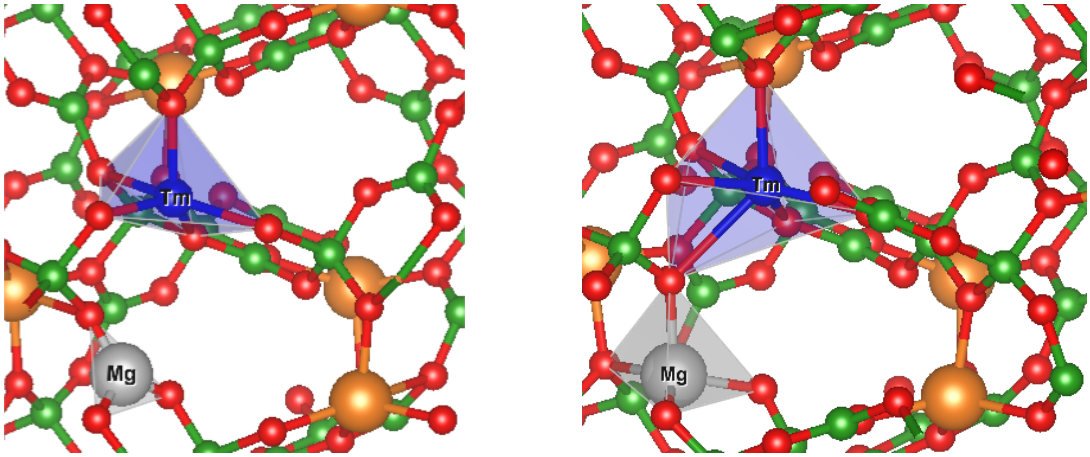

(c) (d)

Figure 4. Configuration with smallest energy cost for both mainly substitutional mechanisms. Figures (a), (c) represent the geometry of defect region before relaxation while (b), (d) represent the final position of the neighbouring ions after relaxation of the lattice. The cuts were made in z-axis for figure (c), (d) while a minimum rotation to the x axis was necessary to see figures (a), (b).

Another important aspect of the result shown in figure 3 is that substitution at the boron site implies a significant displacement not only in the first neighbouring ions, but also in ions of second region. If we consider boron as an ionic atom, the similarity of radii between ions involved in defect scheme (i) is too large and would always give the highest solution energy. On the other hand, the Mg site also has a small ionic radius ($r(Mg^{2+})$ = 66.0 pm, CN = 5 [33]) when compared to ionic radius average for lanthanide ions which implies a high energetic cost for substitution in that site. Furthermore, isovalent substitution typically causes less distortion in the lattice than aliovalent because the material does not need to create extra defect to compensate the excess of charge [16].

Figure 4 was obtained to see the distortion caused by the introduction of dopants in substitutional sites as well as the region closer to the dopant after lattice relaxation and energy minimisation. Figure 4 (a) and (c) show the unrelaxed configuration with the smallest energy cost for substitution in B site scheme and the scheme with Mg anti-site compensation. Figures 4(b) and (d) show the final configurations after lattice relaxation. In both cases, the final configuration brings dopants with coordination number equal 6 which is usual for lanthanide dopants. For direct B substitution, dopant causes an increase in distances between cation and anions neighbors (from 1.51 to 2.41 Å) and, as consequence, a molecule of $(BO_3)^{-3}$ moves to an empty region in of the crystal. For Mg-B anti-site defect, the dopant also causes an increase in distances, from 2.03 to 2.28 Å, but the displacement is lower than substitution at B site.

For both defects present in figure 4(d) and (e), there are displacement or substitution of host elements beyond dopant which implies in configurations with point defects associates. These defects might be considered during interpretation of luminescent mechanism because they can create electronic trapping centers in the material. Therefore, luminescent mechanism models which consider only the inclusion of lanthanide level in the material may not correctly describe the luminescent phenomenon.

IV. CONCLUSIONS

In this work, we used a classical computational modelling approach to describe the intrinsic and extrinsic defects in MgB_4O_7. The description was made by a new set of interatomic potential parameters that consider the Buckingham potential to describe Mg-O and B-O pair interactions plus three-body bond-bending terms used to describe B-O-B bond angles as accurate as possible. The structures were reproduced with discrepancy between experimental and simulated structures better than 2% for MgB_4O_7 and 3.4% for oxide precursor parameters, respectively. The potential parameters also reproduced $(BO_4)^{-5}$ and $(BO_3)^{-3}$ polyhedron structures with discrepancy better than 4% for B-O distances and 5% for angles. Intrinsic defects were initially calculated under unbound condition to obtain the most favourable defect that was further investigated under bound condition to obtain results closer to the real crystal. The results demonstrated that O Frenkel defect is the most probable intrinsic disorder with a Frenkel pair with O in P4 interstitial relaxed position and a O surround by two boron and one magnesium ion is the most probable configuration. A stabilised vacancy is in line with electron paramagnetic resonance (EPR) studies presented in literature. Results from extrinsic defect calculations demonstrated two possible doping mechanisms for lanthanide ions. The first is the direct substitution in boron site with a molecule of $(BO_3)^{-3}$ moving to an empty region in the crystal to balance the strain caused by this substitution. The second is a substitution in magnesium site with a n Mg_B anti-site as charge compensation defect. For both, there are ion displacements beyond first neighbours that shall be considered.

ACKNOWLEDGMENTS

The authors gratefully acknowledge the CNPq, CAPES and FAPITEC/SE, Brazilian funding agencies, and Federal Institute of Sergipe (Edital nº 04/2018/PROPEX/IFS) for financial support. We acknowledge the computer facilities of the Centro Nacional de Processamento de Alto Desempenho (CENAPAD-SP) done under research proposal N°542.

REFERENCES

[1] H.R.B.R. Lima, D.S. Nascimento, E.M. Sussuchi, F. d'Errico, S.O. de Souza, Synthesis of MgB4O7 and Li2B4O7 crystals by proteic sol–gel and Pechini methods, Journal of Sol-Gel Science and Technology. 81 (2017) 797–805. https://doi.org/10.1007/s10971-016-4249-z.

[2] L. Freire de Souza, L.V.E. Caldas, D.O. Junot, A.M.B. Silva, D.N. Souza, Thermal and structural properties of magnesium tetraborate produced by solid state synthesis and precipitation for use in thermoluminescent dosimetry, Radiation Physics and Chemistry. 164 (2019). https://doi.org/10.1016/j.radphyschem.2019.108382.

[3] N. Shrestha, D. Vandenbroucke, P. Leblans, E.G. Yukihara, Feasibility studies on the use of MgB4O7:Ce,Li-based films in 2D optically stimulated luminescence dosimetry, Physics Open. 5 (2020). https://doi.org/10.1016/j.physo.2020.100037.

[4] L.F. Souza, A.M.B. Silva, P.L. Antonio, L.V.E. Caldas, S.O. Souza, F. d'Errico, D.N. Souza, Dosimetric properties of MgB4O7:Dy,Li and MgB4O7:Ce,Li for optically stimulated luminescence applications, Radiation Measurements. 106 (2017) 196–199. https://doi.org/10.1016/j.radmeas.2017.02.009.

[5] V. Pagonis, N. Brown, G.S. Polymeris, G. Kitis, Comprehensive analysis of thermoluminescence signals in MgB4O7:Dy,Na dosimeter, Journal of Luminescence. 213 (2019) 334–342. https://doi.org/10.1016/j.jlumin.2019.05.044.

[6] L.F. Souza, P.L. Antonio, L.V.E. Caldas, D.N. Souza, Neodymium as a magnesium tetraborate matrix dopant and its applicability in dosimetry and as a temperature sensor, Nuclear Instruments and Methods in Physics Research, Section A: Accelerators, Spectrometers, Detectors and Associated Equipment. 784 (2015) 9–13. https://doi.org/10.1016/j.nima.2014.12.030.

[7] E.G. Yukihara, B.A. Doull, T. Gustafson, L.C. Oliveira, K. Kurt, E.D. Milliken, Optically stimulated luminescence of MgB4O7:Ce,Li for gamma and neutron dosimetry, Journal of Luminescence. 183 (2017) 525–532. https://doi.org/10.1016/j.jlumin.2016.12.001.

[8] L.F. Souza, A.L.F. Novais, P.L. Antonio, L.V.E. Caldas, D.N. Souza, Luminescent properties of MgB4O7:Ce,Li to be applied in radiation dosimetry, Radiation Physics and Chemistry. 164 (2019). https://doi.org/10.1016/j.radphyschem.2019.108353.

[9] M.C.L. Moreira, S.O. Souza, M.C. Alves, A.B. de Carvalho, F. d'Errico, Monte Carlo simulations of PVC films loaded with microparticles of MgB4O7 to detect albedo neutrons, Radiation Measurements. 134 (2020) 106322. https://doi.org/10.1016/j.radmeas.2020.106322.

[10] T.M. Oliveira, A.F. Lima, M.G. Brik, S.O. Souza, M. v. Lalic, Electronic structure and optical properties of magnesium tetraborate: An ab initio study, Computational Materials Science. 124 (2016) 1–7. https://doi.org/10.1016/j.commatsci.2016.07.007.

[11] B.A. Doull, L.C. Oliveira, D.Y. Wang, E.D. Milliken, E.G. Yukihara, Thermoluminescent properties of lithium borate, magnesium borate and calcium sulfate developed for temperature sensing, Journal of Luminescence. 146 (2014) 408–417. https://doi.org/10.1016/j.jlumin.2013.10.022.

[12] O. Annalakshmi, M.T. Jose, U. Madhusoodanan, J. Sridevi, B. Venkatraman, G. Amarendra, A.B. Mandal, Thermoluminescence mechanism in rare-earth-doped magnesium tetra borate phosphors, Radiation Effects and Defects in Solids. 169 (2014) 636–645. https://doi.org/10.1080/10420150.2014.918128.

[13] N.K. Porwal, R.M. Kadam, T.K. Seshagiri, V. Natarajan, A.R. Dhobale, A.G. Page, EPR and TSL studies on MgB4O7 doped with Tm: role of BO32− in TSL glow peak at 470K, Radiation Measurements. 40 (2005) 69–75. https://doi.org/10.1016/j.radmeas.2005.04.007.

[14] O. Annalakshmi, M.T. Jose, U. Madhusoodanan, B. Venkatraman, G. Amarendra, Synthesis and thermoluminescence characterization of MgB4O 7:Gd,Li, Radiation Measurements. 59 (2013) 15–22. https://doi.org/10.1016/j.radmeas.2013.10.001.

[15] E.B.V. Freire, A.L. de S. Santos, G.F. da C. Bispo, Z.S. Macedo, M.E.G. Valerio, Computational modeling of intrinsic defects in cadmium silicate, Journal of Physical Chemistry C. x (2019) x.

[16] G.F. da C. Bispo, R.A. Jackson, Z.S. Macedo, M.E.G. Valerio, Ln3+ doping in CaYAl3O7 and luminescence concentration quenching studied via a new computer modelling strategy, Optical Materials. 92 (2019) 212–216. https://doi.org/10.1016/j.optmat.2019.04.036.

[17] E.B. Vaz Freire, A.L. de Sales Santos, G.F. da Cunha Bispo, M. de Andrade Gomes, Z.S. Macedo, R.A. Jackson, M.E.G. Valerio, Intrinsic defects and non-stoichiometry in undoped cadmium silicate hosts, Journal of Alloys and Compounds. (2020) 157580. https://doi.org/10.1016/j.jallcom.2020.157580.

[18] A.L. de S. Santos, E.B. v Freire, G.F. da C. Bispo, Z.S. Macedo, M.E.G. Valerio, Computational modelling of intrinsic defects in the orthosilicates Y2SiO5 and Lu2SiO5, Journal of Physics: Condensed Matter. 31 (2019) 415902. https://doi.org/10.1088/1361-648X/ab2b63.

[19] R.M. Araujo, K. Lengyel, R.A. Jackson, L. Kovács, M.E.G. Valerio, A computational study of intrinsic and extrinsic defects in LiNbO 3, Journal of Physics: Condensed Matter. 19 (2007) 046211. https://doi.org/10.1088/0953-8984/19/4/046211.

[20] M.V. dos S. Rezende, D.J. Santos, R.A. Jackson, M.E.G. Valerio, Z.S. Macedo, Atomistic simulation and XAS investigation of Mn induced defects in Bi12TiO20, Journal of Solid State Chemistry. 238 (2016) 210–216. https://doi.org/10.1016/J.JSSC.2016.03.029.

[21] M.V.S. Rezende, C. Arrouvel, S.C. Parker, J.F.Q. Rey, M.E.G. Valerio, Study of surfaces and morphologies of proteic sol e gel derived barium aluminate nanopowders : An experimental and computational study, Materials Chemistry and Physics. 136 (2012) 1052–1059. https://doi.org/10.1016/j.matchemphys.2012.08.050.

[22] J.D. Gale, GULP: A computer program for the symmetry-adapted simulation of solids, Journal of the Chemical Society, Faraday Transactions. 93 (1997) 629–637. https://doi.org/10.1039/a606455h.

[23] H. Bartl, W. Schuckmann, Zur Struktur des Magnesiumdiborats, MgO(B2O3)2, Neues Jahrbuch Für Mineralogie - Monatshefte. (1966) 142–148.

[24] K. Momma, F. Izumi, VESTA 3 for three-dimensional visualization of crystal, volumetric and morphology data, Journal of Applied Crystallography. 44 (2011) 1272–1276. https://doi.org/10.1107/S0021889811038970.

[25] A. Takada, C.R.A. Catlow, G.D. Price, Computer modelling of B2O3. I. New interatomic potentials, crystalline phases and predicted polymorphs, Journal of Physics: Condensed Matter. 7 (1995) 8659–8692. https://doi.org/10.1088/0953-8984/7/46/003.

[26] J. Roos, C. Eames, S.M. Wood, A. Whiteside, M. Saiful Islam, Unusual Mn coordination and redox chemistry in the high capacity borate cathode Li7Mn(BO3)3, Physical Chemistry Chemical Physics. 17 (2015) 22259–22265. https://doi.org/10.1039/C5CP02711J.

[27] G.E. Gurr, P.W. Montgomery, C.D. Knutson, B.T. Gorres, The crystal structure of trigonal diboron trioxide, Acta Crystallographica Section B Structural Crystallography and Crystal Chemistry. 26 (1970) 906–915. https://doi.org/10.1107/S0567740870003369.

[28] S. Sasaki, K. Fujino, Y. Takeuchi, X-ray determination of electron-density distributions in oxides, MgO, MnO, CoO, and NiO, and atomic scattering factors of their constituent atoms., Proceedings of the Japan Academy, Series B. 55 (1979) 43–48. https://doi.org/10.2183/pjab.55.43.

[29] T.D. Gustafson, E.D. Milliken, L.G. Jacobsohn, E.G. Yukihara, Progress and challenges towards the development of a new optically stimulated luminescence (OSL) material based on MgB4O7:Ce,Li, Journal of Luminescence. 212 (2019) 242–249. https://doi.org/10.1016/j.jlumin.2019.04.028.

[30] G.F.C. Bispo, A.B. Andrade, C. dos S Bezerra, V.C. Teixeira, D. Galante, M.E.G. Valerio, Luminescence in undoped CaYAl3O7 produced via the Pechini method, Physica B: Condensed Matter. 507 (2017) 119–130. https://doi.org/10.1016/j.physb.2016.12.002.

[31] E.G. Yukihara, E.D. Milliken, B.A. Doull, Thermally stimulated and recombination processes in MgB4O 7 investigated by systematic lanthanide doping, Journal of Luminescence. 154 (2014) 251–259. https://doi.org/10.1016/j.jlumin.2014.04.038.

[32] A. Ozdemir, V. Altunal, V. Guckan, K. Kurt, Z. Yegingil, Luminescence characteristics of newly-developed MgB4O7:Ce3+,Na+ phosphor as an OSL dosimeter, Journal of Alloys and Compounds. 865 (2021) 158498. https://doi.org/10.1016/j.jallcom.2020.158498.

[33] R.D. Shannon, Revised effective ionic radii and systematic studies of interatomic distances in halides and chalcogenides, Acta Crystallographica Section A. 32 (1976) 751–767. https://doi.org/10.1107/S0567739476001551.